Journal of The Electrochemical Society, 2023 **170** 047513
1945-7111/2023/170(4)/047513/8/$40.00 © 2023 The Electrochemical Society ("ECS"). Published on behalf of ECS by IOP Publishing Limited

Synergetic Effect of Three-in-One Nanocomposite Based on AuNPs and rGO-MWCNTs for Ultrasensitive Electrochemical Bio-Diagnostic Applications

Mesfin Zewdu,[1,=] Taniya Sandhu,[2,=] Navjeet Kaur,[2] Mulualem Abebe,[1] Femi Olu,[1,z] and Priyanka Sabherwal[2,z]

[1]*Faculty of Material Science, and Engineering, Jimma Institute of Technology, Jimma University, Jimma, Ethiopia*
[2]*National Centre for Nanoscience and Nanotechnology, University of Mumbai, Kolivery Village, Vidya Nagari, Kalina, Santacruz East, Mumbai, Maharashtra 400098, India*

A simple, two-step AuNPs/rGO-MWCNTs nanocomposite fabrication methodology, via drop-casting of rGO-MWCNTs on bare screen printed electrode (SPE) followed by electrodeposition of AuNPs through voltammetric scanning, without using any toxic reducing agents is reported. Each step of the synthesized nanocomposite is characterized using state-of-art spectroscopic and electrochemical methods. Our results demonstrate that the nanostructured AuNPs/rGO-MWCNTs/SPE showed synergistic effects of high electrocatalytic and electron transfer activity, high surface area to volume ratio, that confirms our synthesized material is the best material to fabricate a portable device for rapid, inexpensive, and sensitive electrochemical biosensors. For validation, the fabricated material subjected to electrochemical sensing of BSA protein. Our AuNPs/rGO-MWCNTs nanocomposite exhibited significant and good linear response over 2.5–12.5 μg ml^{-1} BSA concentration range, with sensitivity of 1.723 μAμg ml^{-1} and limit of detection (LOD) 0.23 μg/ml. This portable sensing system with enhanced performance demonstrates great potential for our synthesized AuNPs/rGO-MWCNs/SPE nanocomposite in application of point of care applications, and offers a universal and reliable platform for in biomarker detection.
 [DOI: 10.1149/1945-7111/acca4d]

Manuscript submitted February 14, 2023; revised manuscript received March 22, 2023. Published April 25, 2023.

Supplementary material for this article is available online

The recent advancement in bio-diagnostics using nanomaterials have caught the attention of researchers and industrialists in various fields, including electrochemical sensors, supercapacitors, and biosensors development.[1,2] The use of nanomaterials has advantage of miniaturizing sensors, amplifying signals, or developing new strategies for the immobilization of biomolecules.[2–4] Modification of nanomaterials can in turn increase stability, charge mobility, functional moieties or reactive groups desirable for bio-comatibility and dispersity. Among a wide variety of nanomaterials, reduced graphene oxide (rGO),[5] carbon nanotubes (CNTs),[6,7] titanium dioxide,[8] polyaniline,[9] carbon nanofibers,[10] and metallic nanoparticles[11] were used to fabricate chemically modified electrodes to enhance the sensitivity, selectivity and good electrical conductivity by developing chemical synergies and compatible bio interface for bio-diagnostics applications. Graphene and carbon based nanostructures have recently received special attention due to their unusual structure existing in zero-dimensional (fullerenes, nanospheres, carbon dots, nano diamonds), one-dimensional (CNTs), carbon nanowires, two-dimensional (graphene, GO nanocomposites) and three-dimension (diamond and graphite) each possessing its own unique properties.[12–15] CNTs are of particular interest in electrochemical sensors due to their superior electrical conductivity, chemical stability, large surface area, ability to minimize surface fouling, and possible acceleration of electrochemical reactions.[16,17] There are many applications of carbon nanotubes, typically multi-walled carbon nanotubes (MWCNTs) as nanomaterial modifiers of electrochemical sensing surfaces are reported in literature.[18–20]

Recently, assembling of rGO and MWCNTs as a nanocomposite formed through non-covalent π-π stacking interactions is demonstrated, obtaining higher electrical conductivity and providing a larger specific area compared with pristine rGO or MWCNTs.[21–23] Nanocomposites synthesized from rGO/MWCNTs demonstrate higher electrical conductivity, providing a larger specific area, high electrical analytical properties, and improved chemical stability, as MWCNTs can prevent irreversible agglomeration of graphene and fills the defects on GO to improve electron transfer.[23–25] Previous studies have synthesized nanocomposites integrating gold nanoparticles (AuNPs) with rGO/MWCNTs for an electrochemical biosensor.[23–28] However, they used mostly techniques involving chemical reduction with toxic reducing agents such as thionyl chloride ($SOCl_2$) and [1-ethyl-3 (dimethylamino) propyl] carbodiimide hydrochloride (EDAC) that are toxic, posing health hazards to human health and the environment. Furthermore, these reagents are expensive, and the preparation to composite rGO/MWCNTs with AuNPs may require multiple and time-consuming steps of preparation or more sensitive handling and is not suitable for a large scale of production.

In the current study, we have reported the fabrication of AuNPs/rGO-MWCNTs nanocomposite through an easy, inexpensive, and environmentally friendly approach. Our new approach is based on functionalization & self-interaction of rGO & MWCNTs to eliminate graphitic and/or amorphous carbon components, and other impurities, to improve electron transfer properties, desirable for ultrasensing bio-diagnostics applications. We used two-step fabrication methodology via drop-casting rGO-MWCNTs (equal *w/v*) on bare screen printed electrode (SPE) followed by electrodeposition of AuNPs by voltammetric scanning, without using any other toxic reducing agents (schematic 1). Electrodeposition of AuNPs was achieved by a electrochemical reduction of Au^{3+} to Au^{0} with a high anodic peak, inducing the deposition of AuNPs onto the rGO-MWCNTs/SPE surface. The obtained AuNPs and rGO-MWCNTs nanocomposite showed excellent synergetic effects in significantly improving electron transfer, high electrode surface area, and superior electrocatalytic performance. The spectroscopic and electrochemical behavior demonstrated by Au/rGO-MWCNTs nanocomposite is the best effective ultrasensitive material that can be used to fabricate a portable device for rapid, inexpensive, and sensitive electrochemical biosensors. Furthermore, our synthesized approach demonstrates the possibility to obtain a good AuNPs linked rGO-MWCNTs nanostructured sensor by a simple and green method without using any dangerous chemicals.

Experimental

Materials and methods.— *Chemicals and reagents.*—Reduced graphene oxide (rGO), purity 99%, number of layers 3–6, diameter

[=]Equal contribution.
[z]E-mail: foluemm@gmail.com; priyanka.sabherwal@nano.mu.ac.in

0.8–2 nm, length 1–2 microns; multi-walled carbon nanotubes (MWCNTs), purity 99%, diameter 5–20 nm, length 10 μm; Aspect Ratio (AR; 2000–500; AR_{avg} 1250) both rGO and MWCNTs were purchased from SHILPENT-ENTERPRIS Canada. Gold (III) chloride trihydrate ($AuCl_3.3H_2O$), potassium ferricyanide K3[Fe (CN)6], potassium chloride (KCl), sulphuric acid 96% (H_2So_4), and nitric acid 69% (HNO_3) were purchased from Sigma-Aldrich India. Bovine serum Albumin (BSA) Purity, 98%, was purchased from Sigma-Aldrich. All chemicals were of analytical grade and used as received without any purification, and aqueous solutions were prepared using double distilled water (DDW). Phosphate buffered saline (1 x PBS) was prepared in the lab using chemicals from Himedia, India.

Instruments and electrochemical measurements.—All electrochemical measurements were performed using the METROHM Autolab B.V. potentiostat/galvanostat system (Metrohm Autolab B.V. Kanaalweg 29/G, 3526 KM, Utrecht, the Netherlands, using NOVA 2.1.2 software for data processing, at ambient temperature. A Zensor screen-printed electrode (SPE) TE 100 with a working electrode diameter of 2 mm and an overall dimension of 50 $\times$ 10 mm, a thickness of 0.5 mm, a thickness of coated material of 10 μm, a graphite working electrode and counter electrode, and an Ag/AgCl reference electrode were used in the system. We have investigated the spectroscopic analysis of synthesized nanocomposite using Fourier transform infrared spectroscopy (FTIR). FTIR spectra were recorded in Perkin Elmer "Spectrum Two" FTIR spectrometer. This instrument uses a typical, high-performance, room-temperature $LiTaO_3$ (lithium tantalate) MIR detector, standard optical system with KBr windows for data collection over a spectral range of 8300 $-$ 350 cm^{-1} at a best resolution of 0.5 cm^{-1}, and a standard AVC with optional APV/AVI configuration. During this work, spectra of molecular fingerprint of the sample were recorded within the spectral range from 4000 cm^{-1} to 500 cm^{-1}. Raman spectra were recorded using Renishaw (Gloucestershire, UK) in Via with an Ar + Green laser at 532 nm as the excitation source; laser power was 0.5 MW with the scanning range from 400 to 4000 cm^{-1} to study the quality of rGO. For MWCNTs and rGO-MWCNT sample, laser excitation 514.5 nm as the excitation source was used. The crystallographic information of the sample in this work was determined using XRD machine, Bruker D8 Discover, of model number Bfs03/RoV. The sample was exposed to X-rays from CuKa radiation with $\lambda = 0.154178$ nm at a scan rate of 0.02° s^{-1} operated at 40 kV and 40 mA scanning in the 2θ range of 20°–80°.

Fabrication of rGO-MWCNTs Nanocomposite.—We have conducted pretreatment of the rGO-MWCNTs to eliminate graphitic nanoparticles, amorphous carbon, and metallic impurities, and/or improve the electron transfer properties and/or allow further functionalization. Our pretreatment method involves exposing rGO-MWCNTs (equal w/v) to a mixture of sulfuric acid and nitric acid under sonication for varying periods of time. Briefly, 10 mg of rGO and 10 mg of MWCNTs powder were weighted and added to a beaker that contained double distilled water (DDW), H_2SO_4, and HNO_3 in the ratio of 6:3:1. The solution was sonicated for 90 min to get uniform dispersion, and then it was kept for 12 h for acid treatment. After 12 h of acid treatment, the solution was again sonicated for 60 min, and then it was centrifuged at 10000 RPM for 30 min to separate bundled CNTs, amorphous carbon, trace amounts of oxides from rGO left out during the reducing process of GO, and residual catalytic material, which was washed and sonicated further. This step was repeated three times, and the reaction solution was diluted, filtered, and washed with DDW to remove the residual acid and get pure rGO-MWCNTs nanocomposite. Finally, the product was dried in the hot air oven at 170 °C, after which the powdered sample was obtained and characterised. In parallel, rGO and MWCNTs were prepared separately using the same method of acid treatment to compare their individual crystallinity phases with the nanocomposite synthesized from both rGO-MWCNTs.

The as-synthesized and purified rGO-MWCNTs were characterized with the help of FTIR, XRD, and Raman microscope systems.

Surface modification of SPE by rGO-MWCNTs Nanocomposite.—Briefly, we prepared 1 mg/ml solution of rGO-MWCNTs in DDW and sonicated for 1 hr to get uniform dispersion. Then 7.5 μl of the sample solution was drop-coated on bare SPE working area in a dropwise manner, followed by drying at 60 °C for 15 min, and the mixture was described as rGO-MWCNTs/SPE. The obtained rGO-MWCNTs/SPE electrode was washed carefully with DDW and baked at 60 °C for an hour. The modified electrode was stored at 37 °C–40 °C for further use. We have investigated the electrochemical characteristics of rGO-MWCNTs/SPE using cyclic voltammetry (CV) and electrochemical impedance spectroscopy (EIS) in 0.1 M of KCl solution containing 0.1 M K3[Fe(CN)6] as supporting electrolyte. The CV graph was recorded in the potential range of 1 V to -1V in three cycles with a scan rate of 0.05 v s^{-1}. The EIS plot was conducted in open circuit potential using starting frequency 100 kHz; end frequency 100mHz; number of frequency 10; and amplitude of potential perturbation 10 mV.

Fabrication of AuNPs/rGO-MWCNTs/SPE Nanocomposite.—The fabrication of AuNPs/rGO-MWCNTs/SPE nanocomposite was based on the reduction of the Au (III) complex by sodium citrate. First, we prepared 1 mg/ml stoke solution of gold salt ($AuCl_3.3H_2O$). From this stoke solution, we have taken 30 μl of gold salt solution diluted in 70 μl of DDW, giving us a total of 100 μl of working gold salt solution. Then 100 μl of the gold solution was drop-casted on rGO-MWCNTs/SPE, and the electrodeposition was done using CV with the potential cycling from -1.0 V to 6.0 V at a 0.05 V s^{-1} scan rate 5 times. Gold NPs were gradually formed as the citrate reduced Au^{3+} to Au^0 and finally, AuNPs/rGO-MWCNTs/SPE nanocomposite was formed. AuNPs/rGO-MWCNTs/SPE nanocomposite was washed with 50 μl DDW and dried for 15 min in a 60 °C oven. Nanostructured SPE was stored at room temperature in dry (dehumidified) conditions for further experiments (Supporting Information, S1).

Finally, CV was performed on bare SPE, rGO-MWCNTs/SPE and AuNPs/rGO-MWCNTs/SPE in a redox-active solution of 0.1 M KCl solution containing 0.1 M K3[Fe(CN)6] as a supporting electrolyte. This method was used to understand the electrochemical redox behavior of the material deposited on the working electrode surface.

Electrochemical Impedance Spectroscopy (EIS) was carried out with the frequency range from 100 kHz and 1000 MHz with an AC amplitude of 10 mV. We have investigated the capability of electron transfer of bare SPE, rGO-MWCNTs/SPE and AuNPs/rGO-MWCNTs/SPE using EIS.

Application.—To assess the applicability of the fabricated AuNPs/rGO-MWCNTs/SPE nanocomposite, electrochemical immune assay of BSA protein was performed on the surface of the nanocomposite. We have prepared 1 mg/ml solution of BSA in 0.01 M of 1 x BSA (PH =7.4) and different concentration (2.5 to 12.5 μg ml^{-1}) was drop-coated on the surface of AuNPs/rGO-MWCNTs/SPE. After that cyclic voltammetry (CV), Square wave voltammetry (SWV) and Differential pulse voltammetry (DPV) was performed for all concentrations. Electrochemical response of AuNPs/rGO-MWCNTs/SPE nanocomposite at different concentrations of BSA was probed. All electrochemical assays were performed in the solution of 0.1 M K4[Fe(CN)6] prepared in 0.01 M 1X PBS.

Result and Discussion

Characterization of the AuNPs/rGO-MWCNTs nanocomposite.—We have conducted XRD analysis to examine the crystallinity phase present and to determine the interlayer spacing in the synthesized nanocomposite. The XRD patterns of different

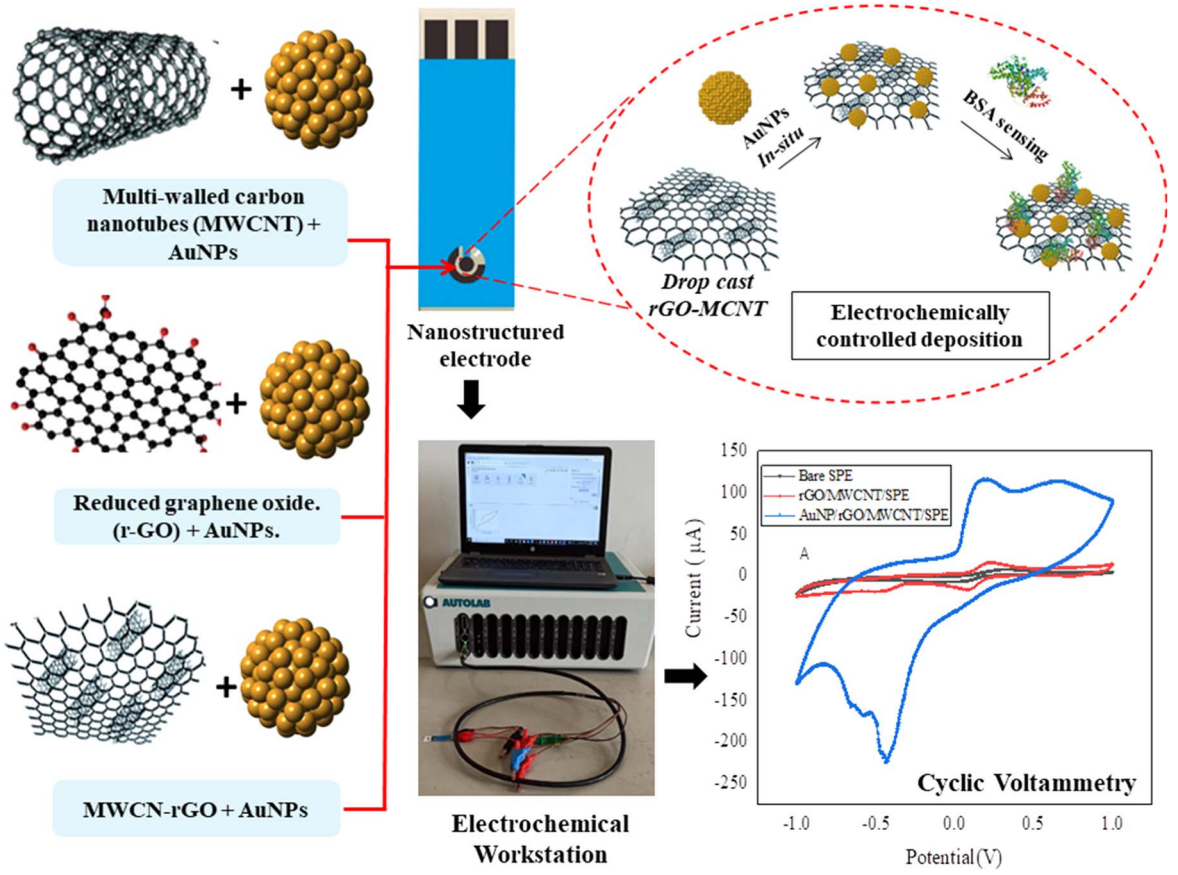

Schematic 1. Procedure of fabricating the material and electrochemical assay of BSA.

materials, including rGO, MWCNTs, and rGO-MWCNTs, are shown in Fig. 1. For rGO, the presence of a broad peak observed at $2\theta = 25.78^0$ indicates that the p-conjugated structure of graphene has been restored considerably in the produced rGO.[29,30] The sharp peak at $2\theta = 25.78^0$ assigned to the plane (002) for rGO implied that the crystal phase (002) was arranged randomly as compared to the high crystallization structure of graphite, where a sharp and intense (002) peak can be observed (Fig. 1). For MWCNTs, the peaks observed at $2\theta = 25.6^0$ and 44.5^0 in the XRD patterns can be assigned to the (0 0 2) and (1 0 0) planes of the hexagonal structure of MWCNTs. The diffraction peak close to $2\theta = 42.4^0$ is characteristic of the face-centered cubic (FCC) crystalline structure in the plane (1 0 0). Similar observations have been made in the literature.[31–34] It can be seen that rGO-MWCNTs displays the peaks at $2\theta = 25.2°$ and $2\theta = 42.7°$ corresponding to (002) and (100) plans that were attributed to the combination of rGO and MWCNTs forms of graphite.[35,36] The XRD spectra of all rGO, MWCNTs, and rGO-MWCNTs showed the same broad peaks at $2\theta = 25.2^0$ confirming

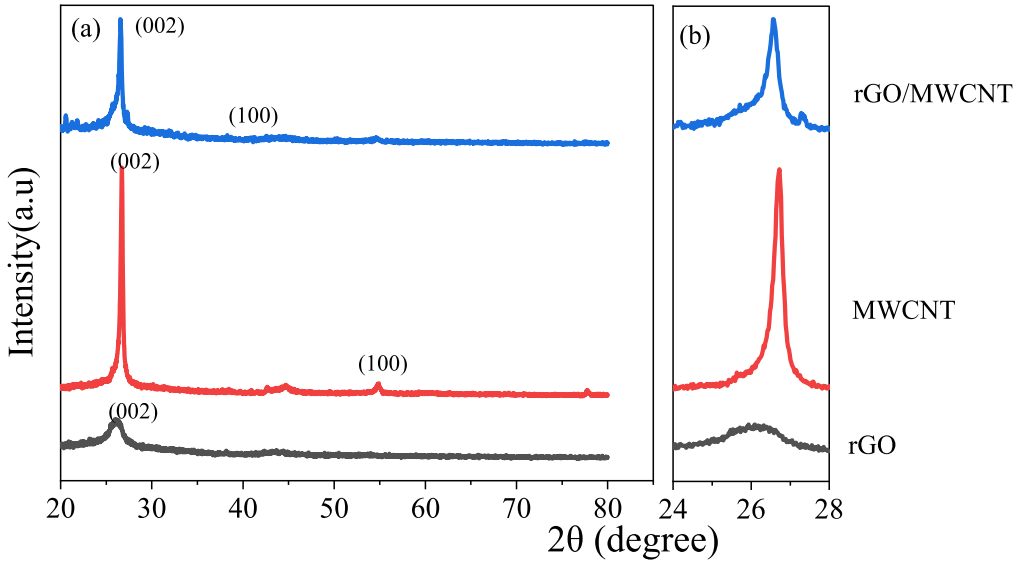

Figure 1. XRD patterns of rGO, MWCNTs, rGO-MWCNTs.

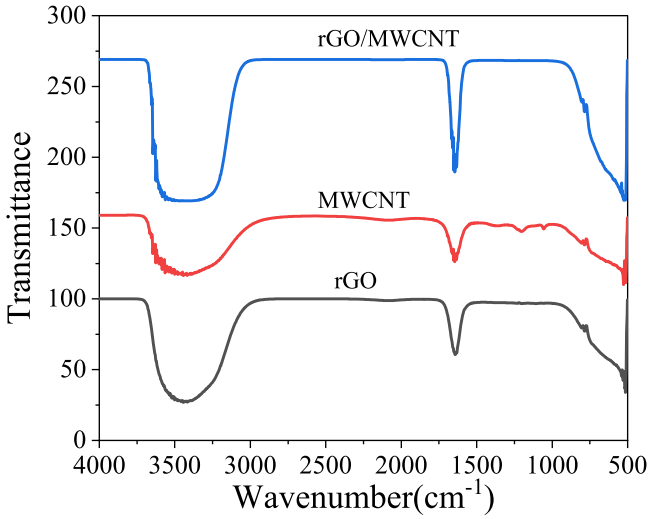

Figure 2. FTIR spectra for: rGO, MWCNT and rGO-MWCNTs.

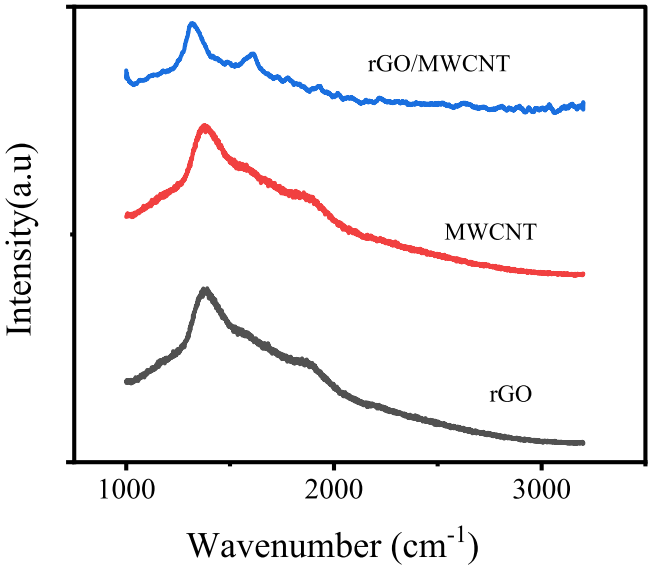

Figure 3. Raman Spectra analysis of rGO, MWCNTs, and rGO-MWCNTs.

rGO is fully incorporated in MWCNTs and forms a stable nanocomposite. Furthermore, our XRD analysis confirmed the nanocomposite structural variations in the components.

In our study, we conducted FTIR spectra analysis for rGO, MWCNTs, and rGO-MWCNTs to investigate the presence of functional groups in the samples from the obtained vibrational (transmittance/absorption) spectra. This analysis is based on the vibrational excitation of molecular bonds by the absorption of infrared light energy,[37,38] within the wavelength range of 4000 to 400 cm^{-1}. Furthermore, FTIR analysis was used to confirm the structural change that occurred during the formation of the rGO-MWCNTs composite. Figure 2 compares the FTIR spectra obtained for the reduced rGO with those of MWCNTs and the rGO-MWCNTs nanocomposite.

As we can see in Fig. 2, the broad peak of rGO at 3454 cm^{-1} proves that the hydroxyl groups pertaing to rGO were removed significantly. It is also noticeable that other peaks were seen at 1839 cm^{-1} due to the removal of oxygen moieties by using hydrazine hydrate during the reduction.[31] Therefore, the oxygen-containing functional groups were successfully removed partially, and the low amounts of residue from functional groups are still remaining at the edge and basal plane of rGO. FT-IR spectrum analysis of the oxidized MWCNTs indicates a dramatic inecrease in the intensities of the peaks corresponding to –COOH stretching vibration peak at 1645cm^{-1} and the–OH deformation vibration peaks (3438 cm^{-1} and 1361 cm^{-1}). The vibration peak at 1545.54 cm^{-1} confirms the presence of the C-C double bond that forms the framework of the carbon nanotube sidewall.[39–41] A strong peak was also observed at 1066.63 cm^{-1}; this is probably associated with the stretching of the sulfoxide bond (S-O), which is usually created in defective MWCNTs areas. A high H_2SO_4 concentration, as reported by Chiang's group, may result in the retention of sulfoxide groups between two free carbons at the end, defect carbons, or two different MWCNTs.[41,42] The strong (large) peak also observed between 3000–3500 cm^{-1} can be attributed to the O-H stretching mode of the carboxyl groups. All rGO, MWCNTs, and rGO/MWCNTs showed a broad peak at 3454 cm^{-1} which was attributed to the stretching vibrations of –OH from C-OH, -COOH groups.[43] The functional groups of the rGO/MWCNTs nanocomposite show similar wide peak at approximately 3500 cm^{-1}, which is attributed to the –OH stretching vibration and carboxyl group. Strong peak at approximately 1630 cm^{-1} is attributed to C = C stretching vibration from the effective sp^2 hybrid region repairing during acid treatment. Therefore, it is confirmed that the acid treatment used in this study can effectively remove most of the oxygen-containing functional groups, as a result, enhancing the electroanlytical and electrical properties of rGO/MWCNTs nanocomposite. Compared to the parent rGO and MWCNs, The peaks at 1030 cm^{-1} for –COOH stretching vibration for MWCNTs, and 97 cm^{-1} for C–OH stretching vibration in the spectra of rGO/MWCNTs become almost invisible indicating that the functional groups have been mostly removed after acid treatment. Thus, our FTIR spectrum analysis confirmed the formation of the rGO-MWCNTs nanocomposite, which agreed with our XRD data.

To further investigate the crystal structures of rGO, MWCNTs, and rGO-MWCNTs as well as the presence of disorder in our sample, we h performed Raman investigations on these materials (Fig. 3). In contrast to MWCNTs, showing peaks at 1371 cm^{-1} D band and 1860cm^{-1} G band, rGO exhibits a high peak at 1381 cm^{-1} D band and a relatively minor peak at 1875cm^{-1}. The peaks representing the disorder-induced D band of rGO and MWCNTs, respectively, emerged at 1381 cm^{-1} and 1371 cm^{-1}, and those representing the crystalline graphitic G band at 1875cm^{-1} and 1860 cm^{-1}.[44,45] For rGO-MWCNTs nanocomosite, the disorder-induced D band peak at 1312 cm^{-1} and the crystalline graphitic G band peak at 1603cm^{-1} was observed. The weak G band peak and diminished intensity of D band peak observed in rGO-MWCNTs clearly indicating that the amorphous carbon is almost completely removed by the purification process. The vibration peaks for rGO and MWCNs are suppressed in the nanocomposite, as can be seen when comparing the Raman spectra of rGO, MWCNTs, and their hybrid rGO-MWCNTs composites. Convolution of the peaks with the more strong D and G bands of MWCNTs and rGO may be the cause of this. Additionally, the shift in peaks points to structural modifications in composites,[45,46] as well as a robust π–π interaction between MWCNTs and rGO, which is apparent from our FTIR spectrum.

The intensity ratio I_D/I_G is typically employed to observe the defects visible in materials connected to graphene.[47] The intensity ratio I_D/I_G increases from 0.7365 for rGO to 0.7371 for MWCNTs and 0.8185 for rGO-MWCNTs. Our findings depicts that synthesized nanocomposite material has more defects than parent moieties, rGO and MWCNTs. The disintegration of oxygen-containing groups, which causes the loss of carbon atoms, is likely what causes the defects to become more pronounced.[48]

Electrochemical characterization of AuNPs/ rGO-MWCNTs/ SPE.—We investigated the electrochemical response during each synthesized step to probe the surface status and posed barrier effects to electron transfer. CV scans of bare SPE, rGO-MWCNTs/SPE, and AuNPs/rGO-MWCNTs/SPE in 0.1 M KCl solution containing 0.1 M

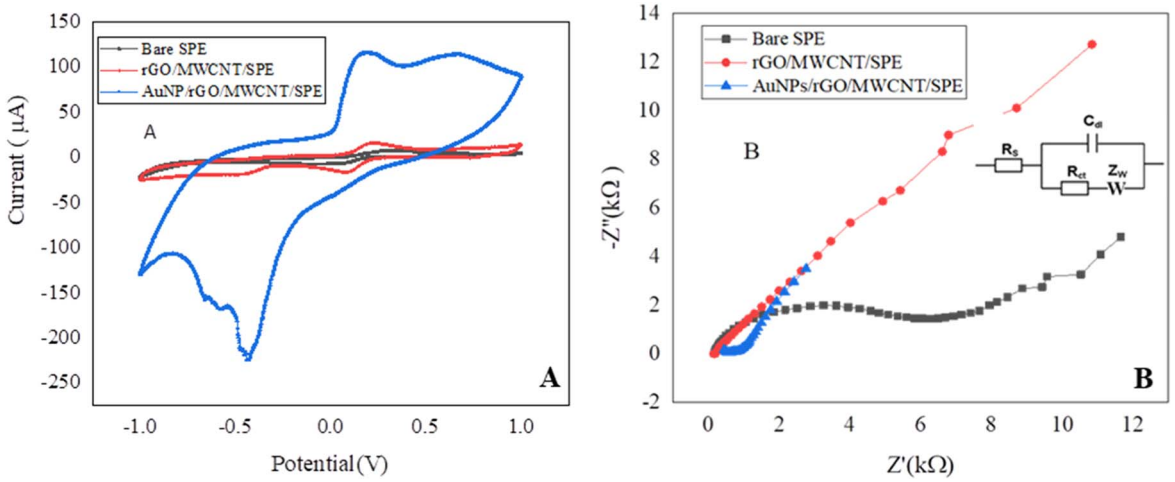

Figure 4. Cyclic voltammograms (A) and Nyquist curves (B) of bare SPE, rGO-MWCNTs/SPE, and AuNPs/rGO-MWCNTs/SPE in 0.1 M KCl solution with 0.1 M K3[Fe(CN)6].

K3 [Fe(CN)6] are shown in Fig. 4. The electrochemical response of bare SPE showed two clear redox peak separations at 0.05 V s^{-1} scan rate, indicating a relatively slow electron transfer and an irreversible electrochemical process.[49] After drop coating with rGO-MWCNTs, there is an increase in redox peak current on the surface of the electrode compared to the bare electrode. This implies that most of the oxygenated groups on rGO-MWCNTs were removed and electron transfer mechanism is enhanced. The electrochemical response including electroactive area was further significantly enhanced after the electrodeposition of AuNPs, which is attributable to excellent electocatalytic ability, and enhanced electrical conductivity of the AuNPs. The increment of electroactive area under CV curve obtained after AuNPs electrodeposited on the surface of rGO-MWCNTs was due to new electrochemical properties, formed by fabricated AuNPs/rGO-MWCNTs nanocomposite. Furthermore, the highest redox peak observed on AuNPs/rGO-MWCNTs/SPE nanocomposite demonstrates a much-enhanced electron transfer process, the synergistic effect of AuNPs/rGO-MWCNTs, and a quasi-reversible electrochemical response, which is in agreement with previously published studies.[49–51]

Electrochemical impedance spectroscopy was used to investigate the interfacial characteristics of the modified electrode. This technique has recently received attention in the field of analytical sciences since it can furnish complementary information about the reaction dynamics and the membrane/solution structure. Nyquist plot semi-circles were fitted using the Randles equivalent circuit model of an electrical circuit that consists of an active electrolyte resistance RS in series with parallel combination of double-layer capacitance C_{dl} and an impedance of a faradaic reaction consisting of an active charge transfer Rct and a specific electrochemical element of diffusion ZW (Fig. 4b). The complex plane spectra of bare SPE, rGO-MWCNTs/SPE, and AuNPs/rGO-MWCNTs/SPE in 0.1 M KCl solution containing 0.1 M K3 [Fe(CN)6] are presented. The fitting value of R_{ct} for bare SPE was 14.6kΩ. After the bare SPE was modified with rGO/MWCNTs, the R_{ct} value dramatically decreased to 2.94kΩ which indicates that the effect of the rGO-MWCNTs nanocomposite on the surface of SPE enhances the conductivity and facilitates electron transfer. After electrodeposition of AuNPs on the surface of rGO-MWCNTs, a big decrease in R_{ct} was observed, showing there is a synergetic effect of these AuNPs and rGO-MWCNTs modifiers, in agreement with our CV results.

We also examined the effect of the aspect ratio, of MWCNs on alignment of AuNPs. The aspect ratio of commercially available MWCNTs, from length-to-diameter ratio (L/d), diameter 5–20 nm, length 10 μm; is (AR; 500–2000-; ARavg 1250). The AuNPs tended to align along the sidewall of the MWNTs with uniform coverage, as is evident from schematic 1. This suggest that higher aspect ratio provide sufficient surface area for the AuNPs to allow their longitudinal adsorption on the MWNTs. It has been reported that longer MWCNTs with higher aspect ratios exhibit better electrochemical

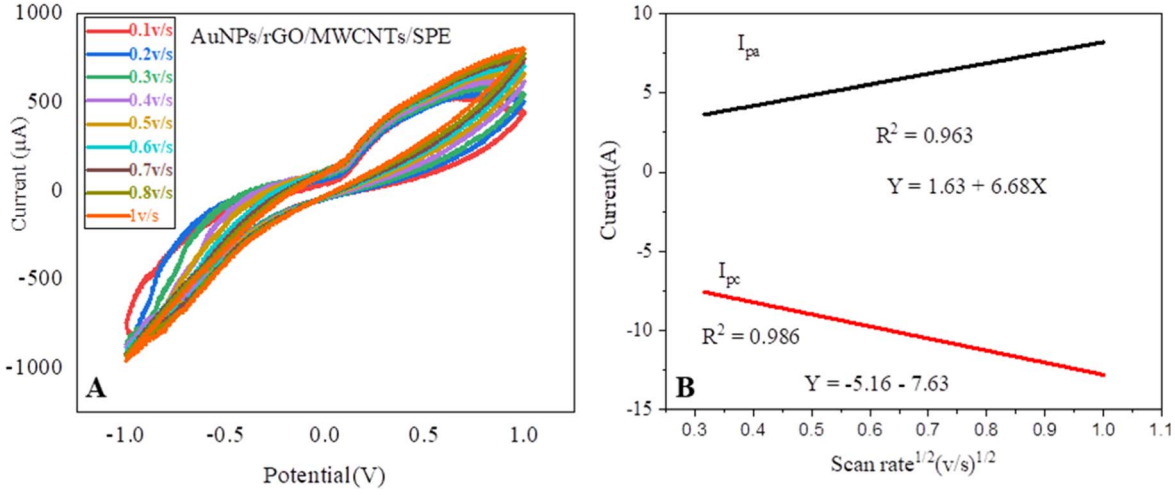

Figure 5. (A) CV scans recorded at different scan rates ranging from 0.1 to 1 v s^{-1} with the square root of scan rates vs peak current for AuNPs/rGO-MWCNTs/SPE in 0.1 M KCl and 0.1 M K3[Fe(CN)6]. (B) Graph between I_{pa} and I_{pc} peak current values and scan rate $(v/s)^{1/2}$.

performance than shorter ones. This is because longer MWCNTs provide a larger surface area for electrochemical reactions to occur, which enhances their electrocatalytic activity. Additionally, MWCNTs with higher aspect ratios also have better electrical conductivity and mechanical strength, which can further improve their electrochemical properties. However, it is important to note that other factors such as surface functionalization and defects can also influence the electrochemical behavior of MWCNTs.

We have carried out scan rate responses of the prepared nanocomposite-modified SPE surface at different scan rates (0.1–1 V s^{-1} at an interval of 0.05 V s^{-1}), as depicted in Fig. 5. As shown in Fig. 5 & S1, we measured the square roots of scan rates $(V/s)^{1/2}$ vs peak current for both AuNPs/rGO-MWCNTs/SPE and rGO-MWCNTs/SPE respectivly. The anodic potential shifts more towards the positive potential and the cathodic peak potential shifts in the reverse direction as we move towards a higher scan rate, implying the system is quasi-reversible.[18] Furthermore, the I_{pa} and I_{pc} peak currents increase linearly with an increase in scan rates $(v/s)^{1/2}$, revealing it as a diffusion-controlled electron transfer process.[52,53] The kinetics of a diffusion-controlled system is defined as the diffusion of ferrocyanide ions from the solution into the interface of the electrode due to a concentration gradient when ions are involved in a redox reaction. By using the Randles-Sevcik equation:

$$I_{peak} = (2.69 \times 10^5)n^{2/3}\mathrm{ACD}^{1/2}V^{1/2} \quad [1]$$

Where Ipeak denotes the anodic peak current, n is the total number of transferring electrons in the redox reaction, A the microscopic surface area of the electrode, D is the ferrocyanate diffusion coefficient, C is the concentration of K3[Fe(CN)6], and v the scan rate in mV/s, with n = 1 and D = 7.26 × $10^{-6}$$cm^2s^{-1}$. Therefore, the effective surface areas were 0.070 cm^2 for bare SPE, 0.129 cm^2 for rGO-MWCNTs/SPE, and 0.138 cm^2 for AuNPs/rGO-MWCNTs/SPE. Our findings indicated that nanocomposite containing rGO-MWCNTs and AuNPs were successfully deposited on the surface of the screen-printed electrode and subsequently increased the active surface area of the electrode compared to bare SPE because both materials had good electrical properties. Furthermore, the highest electrode's electroactive surface area was obtained after being modified with nanocomposites of rGO-MWCNTs and AuNPs, owing to the synergistic impact of the conductivity between rGO-MWCNTs and the AuNPs. The finding from our study is in agreement with studies conducted by different authors.[51–53]

We have further examined the charge transport process of the fabricated nanocomposite; bare SPE, rGO-MWCNTs/SPE and AuNP/rGO-MWCNTs/SPE using electrochemical impedance spectroscopy. The electron transfer rate constant (Ket) values were calculated using Eq. 2.

$$K_{et} = \mathrm{RT}/n^2F^2\mathrm{A}C_OR_{ct} \quad [2]$$

where K_{et} is heterogeneous electron transfer rate constant, R is the gas constant (8.314 J K^{-1} mol^{-1}), T is the temperature in Kelvin degrees, n is the number of electrons, F is Faraday's constant (96.485 C mol^{-1}), A is the electrode surface area in cm^{-2}, C is the redox probe concentration in mol/L, and Rct is the charge transfer

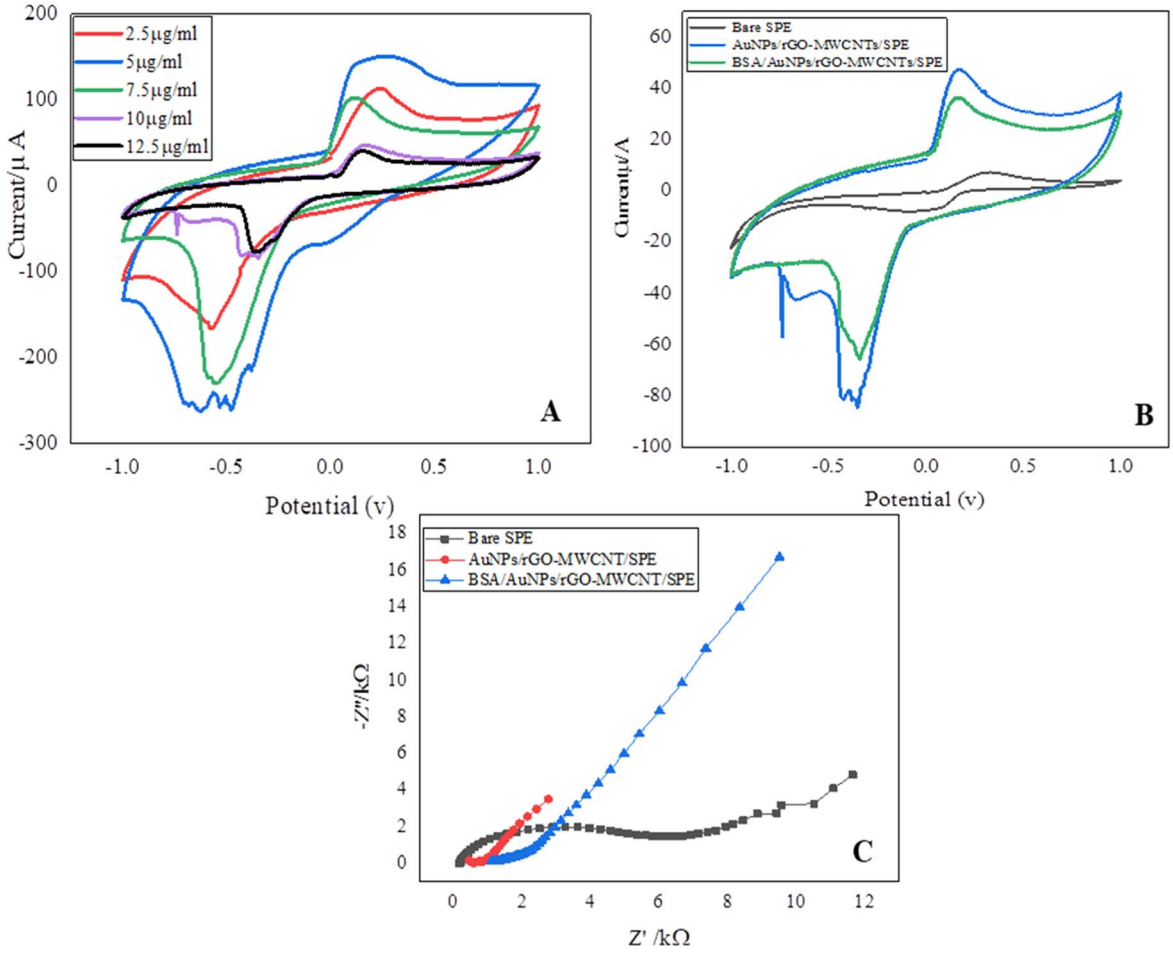

Figure 6. CV response scans of (A). AuNPs/rGO-MWCNs/SPE for different concentration of BSA (B). CV of Bare SPE, AuNPs/rGO-MWCNs/SPE and BSA/AuNPs/rGO-MWCNs/SPE at optimum concentration (C). EIS of Bare SPE, AuNPs/rGO-MWCNs/SPE and BSA/AuNPs/rGO-MWCNs/SPE at optimum concentration.

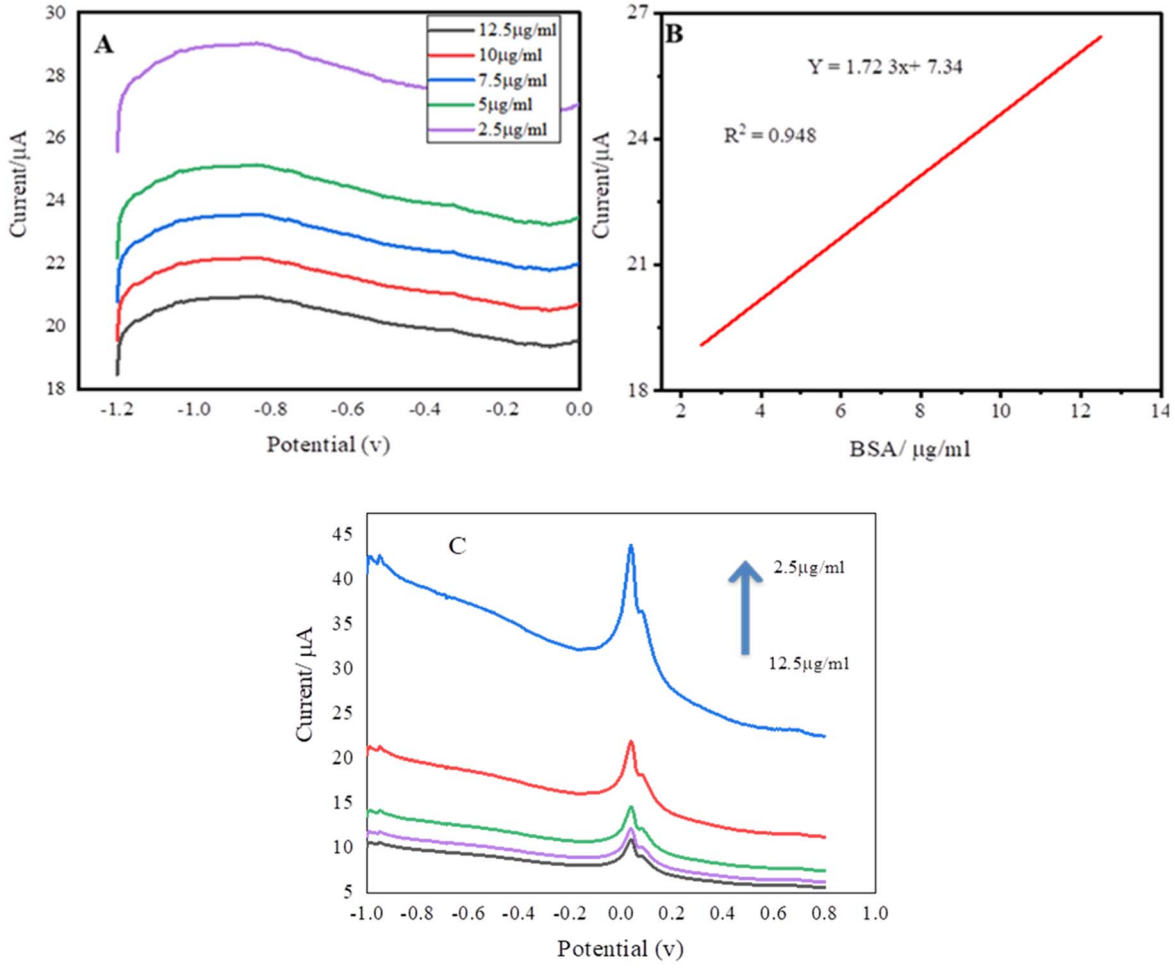

Figure 7. (A) SWV assay of BSA on AuNPs/rGO-MWCNTs/SPE, and (B) Plot of current vs BSA concentration, (C) DPV assay of BSA on the surface of AuNPs/rGO-MWCNTs/SPE.

resistance in Ω, which is determined based on impedance measurements. Findings from our study showed, the electron transfer rate constant (Ket) values, for bare SPE are 0.11 cm^2, for rGO-MWCNTs/SPE 0.13 cm^2, and for AuNPs/rGO-MWCNs/SPE 0.17 cm^2. The highest value in AuNPs/rGO-MWCNTs/SPE indicated a higher rate of electron transfer between the AuNPs/rGO-MWCNTs/SPE interface and redox species, which was consistent with our CV and impedance experiment.

Electrochemical Assays of BSA

To assess the applicability of the fabricated AuNPs/rGO-MWCNTs/SPE nanocomposite, electrochemical immune assay of BSA protein was performed on the surface of the nanocomposite. We have prepared 1 mg ml^{-1} solution of BSA in 0.01 m of 1 × BSA (PH = 7.4). Electrochemical response of AuNPs/rGO-MWCNTs/SPE nanocomposite at different concentration of BSA was probed. As shown in Fig. 7A, CV was recorded for a range of BSA concentration (2.5 μg ml^{-1} to 12.5 μg ml^{-1}). The result indicated that the AuNPs/rGO-MWCNTs/SPE promoted the electrochemical oxidation/reduction of BSA by considerably accelerating the rate of electron transfer and the optimum concentration is 5 μg ml^{-1}, as confirmed by CV technique. In (Fig. 6, as BSA concentrations are increasing, CV response is decreasing, indicating that the presence of a nonconductive biomolecule bound to the sensing surface of nanocomposite is due to the protein adsorption on a gold electrode surface has the effect of blocking the electron transfer between the gold electrode and the aqueous solution. Other Justification could be, BSA has relatively bulky structure, leading to the decrease of the electrons flow and to the huge increase of charge transfer resistance as increasing concentrations. Further, the steric hindrance (slower reaction rate) induced by BSA greatly affects the electrochemical signal which decreases the device sensitivity.[54] As showed in Fig. 7B, less oxidation peak observed at BSA/AuNPs/rGO-MWCNs/SPE than AuNPs/rGO-MWCNs/SPE indicating that the presence of BSA hindered the conductivity features of the sensing layer. As shown in Fig. 7C, the charge-transfer resistance value increased from 1.4kΩfor AuNPs/rGO-MWCNs/SPE to 2.7kΩafter BSA incubated, indicating that the presence of BSA hindered the conductivity features of the sensing layer which is made agreement with our CV result.

Analytical Performance of AuNPs/GO-MWCNs/SPE Nanocomposite.—The response of AuNPs/rGO-MWCNs/SPE electrodes at different concentrations of BSA was probed by square wave voltammetry (SWV). As shown in Fig. 7, scans were recorded for a range of BSA (2.5 μg ml^{-1} o 12.5 μg ml^{-1}). As the concentration of BSA increased, the oxidation peak current of BSA decreseas. A series of SWV responses and the corresponding calibration plots of BSA in the concentration range from 2.5 μg ml^{-1} to 12.5 μg ml^{-1} are shown in Figs. 7A, 7B, respectively. The AuNPs/rGO-MWCNTs/SPE nanocomposite generates an oxidation peak at −1.1 V. The peak position for the oxidation of BSA occurs at lower oxidation potentials, with lowering of the oxidation peak position is indicative of the better catalytic oxidation process of the materials for BSA oxidation. Additionally, the magnitude of the peak current on the SWV curve is proportional to the concentration of BSA. Then, the position of the oxidation peak remained unaltered

with increase in the concentration of BSA. The calibration curve and correlation coefficient were y = 1.723x + 7.34 and R^2 = 0.948 respectively. A significant and good linear relationship between the oxidation peak current and the concentration of BSA was obtained between 2.5 μg ml^{-1} and 12.5 μg ml^{-1} with a sensitivity of 1.723 μAμg ml^{-1}. The detection limit was determined using 3α/slope, where α is the standard deviation of the intercept and s is the slope of the calibration curve, y = 1.723x + 7.34 observed for BSA was 0.23 μg ml^{-1}.

Validation of the AuNPs/rGO-MWCNTs/SPE Nanocomposite at various concentrations of BSA was performed using the DPV technique. Our study showed, as the concentration of BSA increased, the oxidation peak current of BSA increased. The E_p (0.02 V) of BSA remains constant and showed the great stability of our fabricated nanocomposite.

Conclusions

The exploration of facile synthesis, a highly active and cost-effective nanocomposite material for biomaterial application, is an essential job in the area of biosensor development. In this context, it is critical to seek out simple, green, low-cost, and superior electrocatalytic response nanocomposites for practical application. In this work, we have reported the fabrication of AuNPs/rGO-MWCNTs nanocomposite through an easy, inexpensive, and environmentally friendly approach. Our method consists of combining the rGO and MWCNTs powders in proportion and then treating them with H_2SO_4 and HNO_3. We discovered a dried rGO-MWCNTs nanocomposite after acid treatment. After drop casting on bare SPE, electrochemical characterization of the rGO-MWCNTs nanocomposite confirmed the increased surface area of the electrode, improved electron transfer, and chemical stability of the nanocomposite. The formation of rGO-MWCNTs nanocomposite was also confirmed using XRD, FTIR, and Raman spectroscopy analysis. A simple, two-step fabrication of AuNPs/rGO-MWCNTs/SPE was performed. These two-step fabrication methods, via drop-casting of rGO-NWCNTs on bare SPE and then electrodeposition of AuNPs through simple voltammetric scanning, exist without the need for any other toxic reducing agents. Electrodeposition of AuNPs was achieved by a simple reduction of Au^{3+} to Au^0 with a high anodic peak, inducing the deposition of AuNPs onto the rGO-MWCNT/SPE surface. The obtained AuNPs and rGO-MWCNTs nanocomposite showed excellent synergetic effects in significantly improving electron transfer, high electrode surface area, and superior electrocatalytic performance. The spectroscopic and electrochemical behavior demonstrated by AuNPs/rGO-MWCNTs nanocomposite shows it is the best material that can be used to fabricate a portable device for rapid, inexpensive, and sensitive electrochemical biosensors. Furthermore, our synthesized approach demonstrates the possibility to obtain a good AuNPs/rGO-MWCNTs by a simple and green method without using any linker or dangerous chemicals. For validation, the fabricated material subjected to electrochemical immune assay of BSA protein. Our AuNPs/rGO-MWCNTs nanocomposite exhibited significant and good linear response over 2.5–12.5 μg ml^{-1} BSA concentration range, with sensitivity of 1.723 μAμg ml^{-1} and limit of detection (LOD) 0.23 μg ml^{-1}. This proposed composite material can be effectively employed for the development of elcrochemical bio-diagnosic device for point of care detection and the quantification of disease biomakes.

Acknowledgments

The authors are grateful for the research facilities provided by National Center for Nano science and Nano technology (NCNNUM), University of Mumbai, India. Authors are grateful to Biosensika Labs LLP, Mumbai for giving access to Electrochemical workstation procured under BIRAC grant BT/COVID0031/01/20. We also acknowledge the financial support received from Ministry of science and higher education Ethiopia through Embassy of Ethiopia, New Delhi and Jimma University.

ORCID

Mesfin Zewdu https://orcid.org/0000-0002-0256-1608
Femi Olu https://orcid.org/0000-0002-6069-7968
Priyanka Sabherwal https://orcid.org/0000-0001-5331-7894

References

1. M. Nasrollahzadeh, S. M. Sajadi, M. Sajjadi, and Z. Issaabadi, *Interface Science and Technology*, **43**, 113 (2019).
2. Z. Altintas, *Hoboken* (NJ, USA, Wiley) (2017).
3. J. Lei and H. Ju, *Chem. Soc. Rev.*, **41**, 2122 (2012).
4. W. Putzbach and N. J. Ronkainen, *Sensors*, **13**, 4811 (2013).
5. A. Krittayavathananon, P. Srimuk, S. Luanwuthi, and M. Sawangphruk, *Anal. Che*, **86**, 12272 (2014).
6. B. Haghighi, H. Hamidi, and S. Bozorgzadeh, *Anal. Bioanal.Chem.*, **398**, 1411 (2010).
7. Y. Shen, Q. Xu, H. Gao, and N. Zhu, *Electrochem. Commun.*, **11**, 1329 (2009).
8. Q. Yi, F. Niu, and W. Yu, *Thin Solid Films*, **519**, 3155 (2011).
9. H. Lin, J. Yang, J. Liu, Y. Huang, J. Xiao, and X. Zhang, *Electrochim. Acta*, **90**, 382 (2013).
10. H. Zhang, J. Huang, H. Hou, and T. You, *Electroanalysis*, **21**, 1869 (2009).
11. V. Bhalla, S. Carrara, P. Sharma, Y. Nangia, and C. R. Suri, *Sensors & Actuators B*, **161**, 761 (2012).
12. A. K. Sundramoorthy and S. Gunasekaran, *Trends Analyt Chem*, **60**, 36 (2014).
13. J. Yang, J. R. Strickler, and S. Gunasekaran, *Nanoscale*, **4**, 4594 (2012).
14. J. Yang, J. H. Yu, J. Rudi Strickler, W. J. Chang, and S. Gunasekaran, *Biosens. Bioelectron.*, **47**, 530 (2013).
15. H. Ma, G. Wu, Z. Cui, Y. Li, Y. Zhang, and B. Du, *Anal. Lett.*, **46**, 1 (2013).
16. T. Guinovart, M. Parrilla, G. A. Crespo, F. X. Rius, and F. J. Andrade, *Analyst*, **138**, 5208 (2013).
17. A. C. Power, B. Gorey, S. Chandra, and J. Chapman, *Nanotechnol Rev*, **7**, 19 (2018).
18. M. M. Barsan, M. E. Ghica, and C. M. A. Brett, *Anal. Chim. Acta*, **881**, 1 (2015).
19. M. E. Ghica, G. M. Ferreira, and C. M. A. Brett, *J. Solid State Electrochem.*, **19**, 2869 (2015).
20. D. Kul, M. E. Ghica, R. Pauliukaite, and C. M. A. Brett, *Talanta*, **111**, 76 (2013).
21. V. Mani, B. Dinesh, S. M. Chen, and R. Saraswathi, *Biosens. Bioelectron.*, **53**, 420 (2014).
22. J. Hu, Z. Zhao, J. Zhang, G. Li, P. Li, and W. Zhang, *Appl. Surf. Sci.*, **396**, 523 (2017).
23. S. Hashemzadeh, Y. Omidi, and H. Rafii-Tabar, *Mikrochim. Acta*, **186**, 680 (2019).
24. M. Q. Zhao, X. F. Liu, Q. Zhang, G. L. Tian, J. Q. Huang, and W. Zhu, *ACS. Nano*, **6**, 10759 (2012).
25. G. P. Nikoleli, S. Karapetis, S. Bratakou, D. P. Nikolelis, N. Tzamtzis, and V. N. Psychoyios, *Hoboken* (NJ, USA, Wiley) p. 427 (2017).
26. Y. C. Wang, D. Cokeliler, and S. Gunasekaran, *Electroanalysis*, **27**, 2527 (2015).
27. A. Fei, Q. Liu, J. Huan, J. Qian, X. Dong, and B. Qiu, *Biosens. Bioelectron.*, **70**, 122 (2015).
28. S. Akbarzadeh, H. Khajehsharifi, and S. Hajihosseini, *Biosensors*, **12**, 468 (2022).
29. S. Thakur and N. Karak, *Carbon N Y*, **50**, 5331 (2012).
30. P. Cui, J. Lee, E. Hwang, and H. Lee, *Chem. Commun.*, **47**, 12370 (2011).
31. F. W. Low, C. W. Lai, and S. B. Abd Hamid, *Ceram. Int.*, **41**, 5798 (2015).
32. K. J. Chen, K. C. Pillai, R. J. Pan, C. J. Wang, and S. H. Liu, *Biosens. Bioelectron.*, **33**, 120 (2012).
33. H. Allouche and M. Monthioux, *Carbon NY*, **43**, 1265 (2005).
34. T. Edwin, R. Mombeshora, O. Vincent, and P. G. S. Nyamori, *Afr. J. Chem*, **68**, 153 (2015).
35. M. Gopiraman, S. G. Babu, R. Karvembu, and I. S. Kim, *Appl. Catal. A. Gen*, **484**, 84 (2014).
36. M. G. Hosseini and E. Shahryari, *Ionics*, **25**, 2383 (2019).
37. M. Taha et al., *Sci. Med*, **1**, 15 (2013).
38. B. S. He and S. S. Yan, *Anal. Methods*, **10**, 783 (2018).
39. A. Azadbakht, M. Roushani, A. R. Abbasi, and Z. Derikvand, *Anal. Biochem.*, **512**, 58 (2016).
40. S. Rabai, A. Teniou, G. Catanante, M. Benounis, J. L. Marty, and A. Rhouati, *Sensors*, **22**, 105 (2021).
41. K. Saeedfar, L. Y. Heng, and C. P. Chiang, *Bioelectrochemistry*, **118**, 106 (2017).
42. R. S. Nicholson, *Anal. Chem.*, **37**, 1351 (1965).
43. Y. Tang and J. Gou, *Mater. Lett.*, **64**, 2513 (2010).
44. J. H. Lehman, M. Terrones, E. Mansfield, K. E. Hurst, and V. Meunier, *Carbon*, **49**, 2581 (2011).
45. K. Prakash Chandra Mahakul and B. V. R. S. Bamadev Das, *J. Mater. Sci.*, **52**, 5696 (2017).
46. G. Guan, Z. Yang, L. Qiu, X. Sun, Z. Zhang, and Z. Ren, *J. Mater. Chem. A*, **1**, 13268 (2013).
47. X. Gao and X. Tang, *Carbon*, **76**, 133 (2014).
48. J. Yan, Q. Wang, T. Wei, L. Jiang, M. Zhang, and X. Jing, *ACS. Nano*, **8**, 4720 (2014).
49. H. Yu, R. Li, and K. L. Song, *Mikrochim. Acta*, **186**, 624 (2019).
50. Y.-C. Wang, D. Cokeliler, and S. Gunasekaran, *Electroanalysis*, **27**, 2527 (2015).
51. K. Arora, M. Tomar, and V. Gupta, *Biosens. Bioelectron.*, 08 (2017).
52. R. K. Srivastava, S. Srivastava, T. N. Narayanan, B. D. Mahlotra, R. Vajtai, and P. M. Ajayan, *ACS. Nano*, **6**, 168 (2012).
53. K. Jindal, K. M. Tomar, and V. Gupta, *Biosens. Bioelectron.*, **38**, 11 (2012).
54. S. Bonaldo, L. Franchin, E. Pasqualotto, E. Cretaio, C. Losasso, and A. Peruzzo, *IEEE Sens. J.*, **23**, 1786 (2023).